Supporting Information: A Non-Perturbative, Low Noise Surface Coating for Sensitive Force-Gradient Detection of Electron Spin Resonance in Thin Films

Michael C. Boucher, Corinne E. Isaac, Peter Sun, Peter P. Borbat, and John A. Marohn*

Department of Chemistry and Chemical Biology, Ithaca, New York 14853

E-mail: jam99@cornell.edu

Characterization of Tip Magnetic Moment *via* Cantilever Magnetometry

Frequency-shift magnetometry was used to evaluate magnet quality following Ng *et al.*[1,2] Experiments were carried out at a temperature of $T = 4.2\,\mathrm{K}$ and a pressure of $P \leq 1 \times 10^{-5}\,\mathrm{mbar}$, with the cantilever positioned $80\,\mu\mathrm{m}$ above the sample. The external field B_0 was varied between -5 and $5\,\mathrm{T}$. Before data was taken at each B_0, the cantilever drive amplitude was set to 164 nm and the laser temperature adjusted so the cantilever interferometer was centered on-fringe. At each B_0, the cantilever frequency f_m, quality factor Q, and dissipation constant Γ were obtained *via* a ringdown measurement.

The resulting magnetometry data were analyzed using Eqs. 1 through 3 from Ng *et al.*,[1] with

an added diamagnetic frequency shift parameter, c:

$$f_{\mathrm{m}} - f_0 \approx \Delta f \frac{B_0 \Delta B}{B_0 + \Delta B} + c|B_0| \tag{1}$$

with

$$\Delta f = \frac{f_0}{2k_0}\left(\frac{\alpha}{l}\right)^2 \mu \tag{2}$$

and

$$\Delta B = \mu_0 \mu \frac{\Delta N}{V}. \tag{3}$$

In these equations f_0 is the cantilever frequency at B_0 = 0 T, k_0 is the cantilever spring constant at B_0 = 0 T, $\alpha = 1.377$, l is the cantilever length, μ is the tip magnetic moment, V is the tip volume, $\mu_0 = 4\pi \times 10^{-7}\,\mathrm{T\,m\,A^{-1}}$ is the permeability of vacuum, and ΔN is the difference between the demagnetization factors along the direction of the cantilever's width and length. We obtained ΔB, Δf, and c from a fit of the relative frequency shift $f_{\mathrm{m}} - f_0$ *vs.* B_0 data to Eq. 1. The curvature of the plots gives ΔB which, according to Eq. 3, constrains the product of $B_{\mathrm{sat}} = \mu\mu_0/V$ and ΔN. We determined ΔN from magnet dimensions, obtained from scanning electron microscopy, using published formulas for rectangular-prism demagnetization factors.[3]

Frequency-shift cantilever magnetometry data for cantilevers A and B are shown in Fig. S1. See Table S1 for a summary of fit results, including the coercive field H_{c} obtained from the hysteresis curve. The trend of increasing coercive field with reduced magnet diameter is consistent with measurements on magnetic nanorods in the literature, where it has been shown that fine particles can have coercivities orders of magnitude higher than bulk materials.[4,5]

Table S1: Cantilever magnetometry best-fit parameters for cantilevers A and B from the data in Figure S1. The coercive field H_{c} was obtained from the field at which the frequency jump occurs in the hysteresis curve.

Cantilever	ΔB [T]	Δf [Hz/T]	c [mHz/T]	H_{c} [mT]
A	0.36 ± 0.03	2.0 ± 0.1	149 ± 6	100
B	0.81 ± 0.07	2.48 ± 0.07	40 ± 20	60

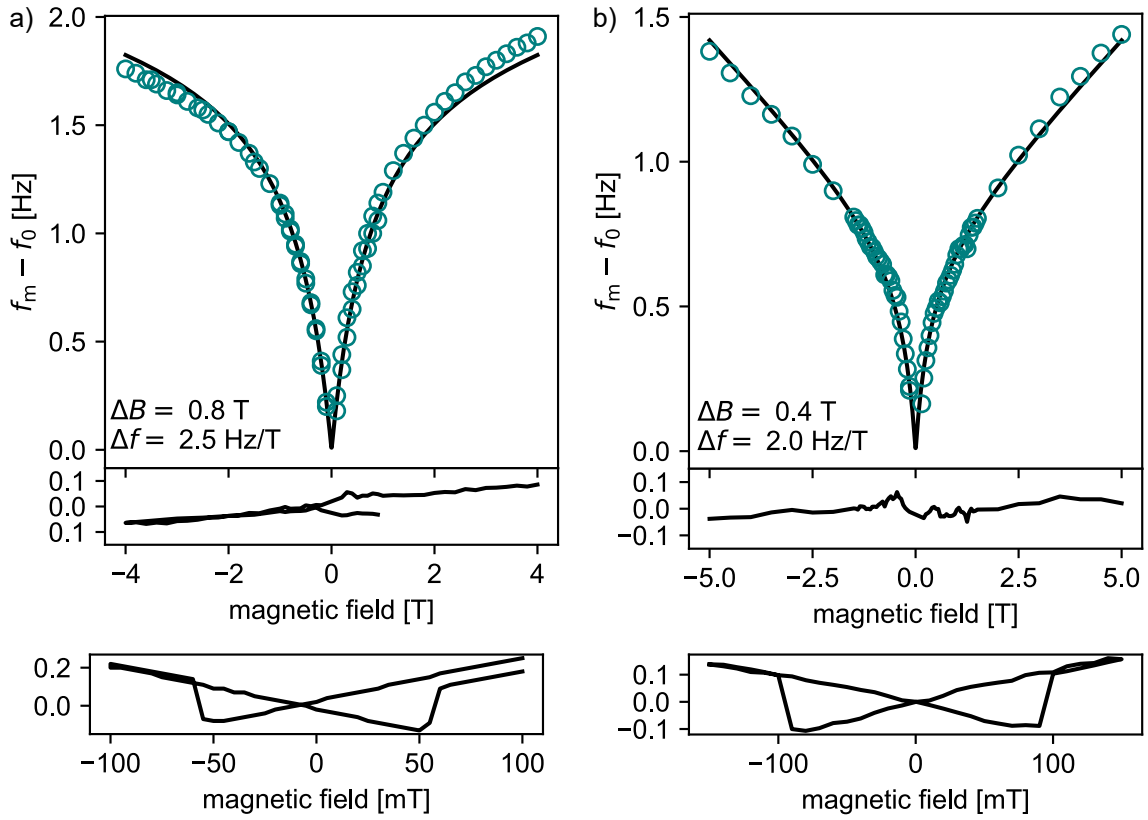

Figure S1: Frequency-shift cantilever magnetometry studies of cobalt-tipped cantilevers, (a) cantilever B and (b) cantilever A, along with best-fit parameters, ΔB and Δf. Data was acquired with the cantilever located 80 µm from the sample surface. Upper: fit to Eq. 1; middle: fit residuals; and lower: magnified view of frequency-shift hysteresis at low field.

Table S2: Cantilever B magnet parameters derived from Fig. S1(a) assuming various uniform damage-layer thicknesses d and fit parameters $\Delta B = (0.81 \pm 0.07)\,\mathrm{T}$ and $\Delta f = (2.48 \pm 0.07)\,\mathrm{Hz}$.

			damage		
parameter	symbol	unit	none	mild	moderate
damage layer thickness	d	nm	0	5	15
magnet volume	V	$10^6\,\mathrm{nm}^3$	16.2	13.0	7.72
difference in demag. factor	ΔN		0.564	0.580	0.622
magnetic moment	μ	$10^{-15}\,\mathrm{Am}^2$	19.	15.	8.0
saturation magnetization	B_{sat}	T	1.4	1.4	1.3
cantilever spring constant	k_0	$10^{-3}\,\mathrm{Nm}^{-1}$	1.3	1.0	0.56

Table S3: Cantilever A magnet parameters derived from Fig. S1(b) assuming various uniform damage-layer thicknesses d and fit parameters $\Delta B = (0.36 \pm 0.03)\,\mathrm{T}$ and $\Delta f = (2.0 \pm 0.1)\,\mathrm{Hz}$.

			damage		
parameter	symbol	unit	none	mild	moderate
damage layer thickness	d	nm	0	5	15
magnet volume	V	$10^6\,\mathrm{nm}^3$	10.5	8.05	4.12
difference in demag. factor	ΔN		0.385	0.379	0.356
magnetic moment	μ	$10^{-15}\,\mathrm{Am}^2$	7.9	6.1	3.3
saturation magnetization	B_{sat}	T	0.94	0.95	1.02
cantilever spring constant	k_0	$10^{-3}\,\mathrm{Nm}^{-1}$	0.68	0.53	0.29

We expect $\Delta B = B_{\mathrm{sat}}\,\Delta N$. For cobalt, we expect $B_{\mathrm{sat}} = 1.8\,\mathrm{T}$, giving $\Delta B = 1.02\,\mathrm{T}$ for cantilever B and $\Delta B = 0.69\,\mathrm{T}$ for cantilever A. The observed ΔB values, $(0.81 \pm 0.07)\,\mathrm{T}$ for cantilever B and $(0.36 \pm 0.03)\,\mathrm{T}$ for cantilever A, were thus significantly smaller than expected. In Tables S2 and S3 we assume a damage layer of non-magnetic material of thickness $d = 0$, 5, and 15 nm on each magnet face. The damage layer decreases the magnetic volume V and demagnetization factor term ΔN. Using the reduced V and ΔN, the tip magnetization μ is recomputed from the observed ΔB using Eq. 3 and the saturation magnetization is recomputed using $B_{\mathrm{sat}} = \Delta B \big/ \Delta N$. From the new tip magnetization μ and measured Δf we compute a cantilever spring constant k_0 using Eq. 2.

For each cantilever the spring constant was independently inferred from Brownian motion measurements, accounting for the fact that cantilever displacement was measured at a reflective pad located some distance from the cantilever tip (where the spin force is applied). The Brownian-motion spring constant was $1.0\,\mathrm{mN\,m}^{-1}$ for cantilever B and $0.8\,\mathrm{mN\,m}^{-1}$ for cantilever A. These measured values are in good agreement with $k_0^{\mathrm{calc}} \sim 1.0\,\mathrm{mN\,m}^{-1}$ calculated from the Young's modulus of silicon and measured cantilever dimensions[6] (340 nm thick, 4 µm wide, 200 µm long, $\langle 1\,0\,0 \rangle$-oriented Si).

For cantilever B, the inferred k_0 is consistent with the measured spring constant for $d \leq 5\,\mathrm{nm}$; in this scenario the inferred saturation magnetization $B_{\mathrm{sat}} = 1.4\,\mathrm{T}$, somewhat lower than the expected

1.8 T. For cantilever A, the inferred k_0 is consistent with a zero-thickness damage layer and a saturation magnetization $B_{\mathrm{sat}} = 0.94\,\mathrm{T}$, approximately half of the expected value. In summary, the magnetometry data is consistent with little or no damage layer but a reduced saturation magnetization.

Partial Saturation from Time-Dependent Resonance Offset

Below we consider the loss of signal due to breakdown of saturation in a moving-tip experiment.

In a separate manuscript in preparation we derive transient solutions to the Bloch equations. These solutions are analytically tractable in the "weak irradiation" limit where $B_1 \leq B_1^{\mathrm{crit}}$, with $B_1^{\mathrm{crit}} = (1/T_2 - 1/T_1)/(2\gamma_{\mathrm{e}}) = 6.3\,\mu\mathrm{T}$ a critical field above which spin nutation is observed; when $B_1 \leq B_1^{\mathrm{crit}}$ the Bloch-equation eigenvalues are real for resonant irradiation. In this limit, we obtain the following expression for the spin-equilibration rate.

$$r(t) = r_1 + \frac{\gamma_e^2 B_1^2 T_2}{1 + \Omega^2(t)} \tag{4}$$

with $\Omega(t) = T_2(\gamma_{\mathrm{e}} B_z(t) - \omega_{\mathrm{res}})$ a unitless resonance offset. If the tip-field is changing linearly in time as spins pass through resonance, we can calculate the fraction of magnetization remaining after a single microwave pulse lasting from time t_{i} to t_{f} by integrating the magnetization equations of motion. We find

$$\frac{M_z(t_{\mathrm{f}})}{M_z(t_{\mathrm{i}})} \approx e^{-R(t_{\mathrm{f}},t_{\mathrm{i}})} \tag{5}$$

with

$$R(t_{\mathrm{f}},t_{\mathrm{i}}) \approx \frac{\gamma_{\mathrm{e}} B_1^2}{|B_{\mathrm{zx}} v_{\mathrm{tip}}|} \left|\arctan(\Omega(t_{\mathrm{f}})) - \arctan(\Omega(t_{\mathrm{i}}))\right| \tag{6}$$

where γ_{e} is the electron gyromagnetic ratio, $B_{\mathrm{zx}} = dB_{\mathrm{z}}/dx$, and v_{tip} is the tip velocity during the microwave sweep. Knowing the fraction of the magnetization remaining after a single microwave sweep and assuming each spin experiences negligible T_1 relaxation while it is passing through

the resonant slice, we are able to derive an average, steady-state magnetization after multiple microwave pulses of

$$M_{z,\mathrm{avg}} = M_0 - \frac{M_0 T_1 (1 - e^{-\frac{\Delta t}{T_1}})(1-x)}{\Delta t\,(1 - x e^{-\frac{\Delta t}{T_1}})} \tag{7}$$

where Δt is the time between microwave pulses and $x = M_z(t_\mathrm{f})/M_z(t_\mathrm{i})$, the ratio of final to initial magnetization following microwave irradiation.

When the magnet tip's radius is smaller than the cantilever's peak-to-peak amplitude, dB_z/dx varies significantly over the cantilever cycle and can no longer be assumed constant. To better approximate signal in the limit of large cantilever amplitude, we break the microwave pulse into smaller time segments represented by individual pairs of grid points in x, the direction of the cantilever motion. We apply Eq. 6 across each pair of points during the cantilever sweep and use the value of dB_z/dx occurring during that segment.

In Fig. S2 we show the effect of time-dependent offset on the simulations of Fig. 6. Figure S2(a) shows the simulation result at $h = 32\,\mathrm{nm}$ presented in red, with a few different external field values marked with black dots. The dotted line represents the signal we would expect if active spins were fully saturated by microwaves.

The sample spins that experience the highest magnetic field gradient and therefore the poorest saturation are in resonance at $B_0 = 285\,\mathrm{mT}$. As we can see from the plotted cross section we expect spins that see this high gradient and only pass through resonance once during the microwave pulse will have an average polarization of around 90% of the Boltzmann polarization. However, the resonant slice has a diameter of only around 100 nm at the sample surface, so many spins pass through resonance twice and end up with an average polarization of around 80%. Other spins remain at or near resonance longer and become even more saturated. In the end we expect a frequency shift of $-22\,\mathrm{mHz}$, a significant fraction of the $-75\,\mathrm{mHz}$ we would expect for fully saturated spins.

We also present cross sections of average expected polarization at $B_0 = 465\,\mathrm{mT}$, near the max-

imum signal for the local peak; and $B_0 = 500\,\mathrm{mT}$, part of the bulk peak. These higher external field values result in a resonant slice with a smaller field gradient and therefore better saturation. Fewer spins pass through resonance twice during the cantilever cycle, although we do start to see more saturation of spins that never pass through resonance, due to the reduced field gradient.

Figure S3 shows the fraction of saturation remaining after a single microwave pulse, used to calculate the results in Figure S2 through Equation 7. On the right side of Figure S3 we plot the results of select grid points of each simulation (dashed lines) to the results of a numerical integration of the full Bloch equations calculated using the `odeint` method from the SciPy Python package with a 10 ps time step (blue lines).

The points we sample are a mixture of more typical active spins (A, C, E, G, I and K) which contribute most of the signal, and less typical spins at the boundaries of the detection volume (B, D, F, H, J and L) which are more likely to challenge the assumptions of our approximation. The analytical approximation we are using does not capture the Rabi oscillations apparent within a few microseconds of reaching resonance but performs decently well for the spins experiencing the largest gradients (A and C), for which higher microwave power would be desirable to improve saturation. The simulation also handles situations such as when the spin passes through resonance more than once (B, D, and H) decently well. The analytical approximation appears most questionable where the gradient is quite weak and spins spend a long time near resonance (I, J, K and L); however, these spins tend towards the same near-zero average saturation value at steady-state regardless of the exact result of a single pulse (notice the relatively uniform coloration of Fig. S2(d)).

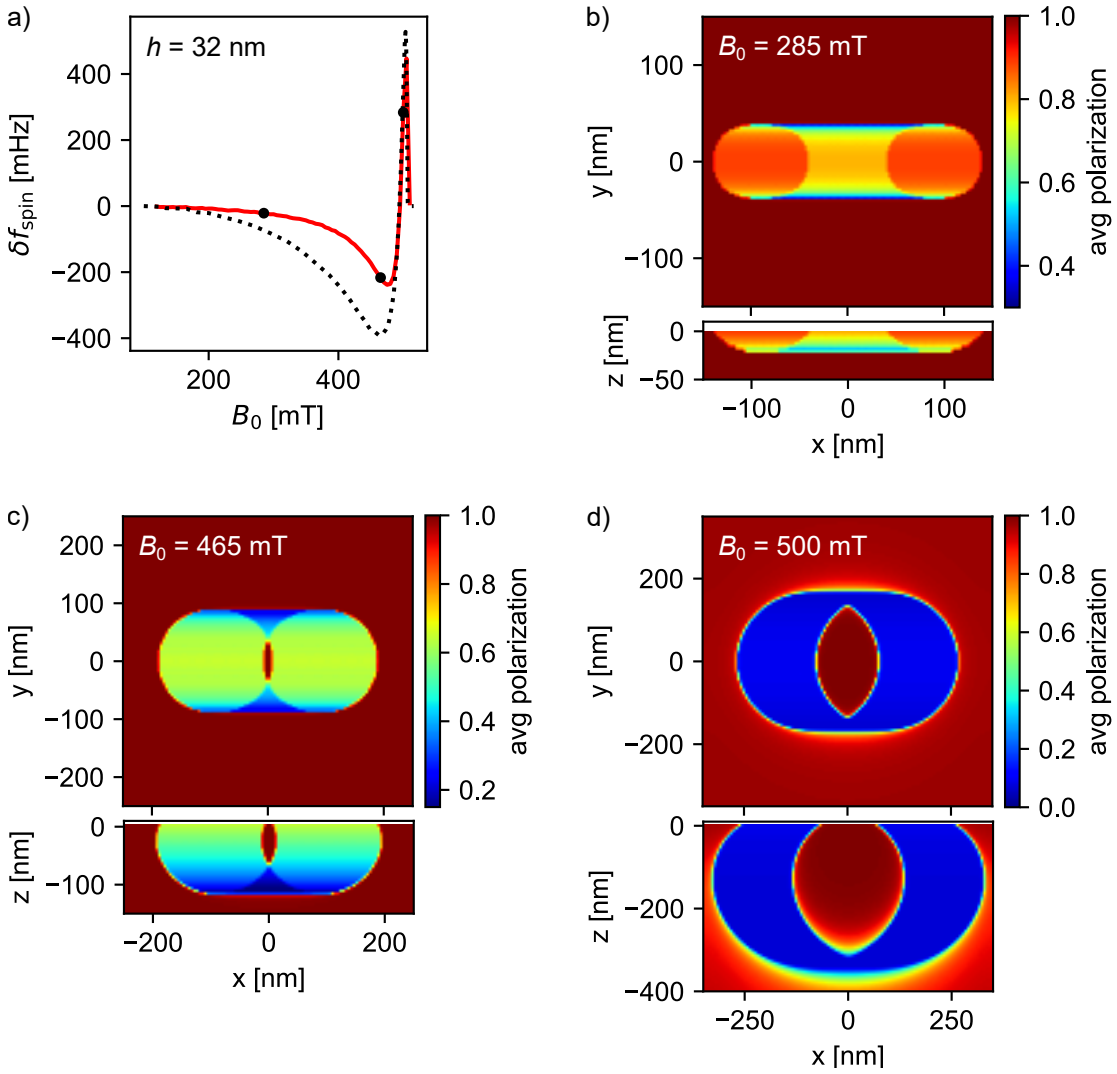

Figure S2: Tip motion creates a time-dependent resonance offset which decreases the achievable spin saturation and the MRFM-ESR signal. (a) Solid red line: simulated ESR signal at $h = 32\,\text{nm}$ including effects of incomplete saturation (see Fig. 6). Dotted black line: the expected signal if active spins are fully saturated. (b-d) Maps of the average polarization at fields indicated by black dots in (a). Upper: average polarization (x, y) cross section for the top layer of the sample. Lower: average polarization (x, z) cross section centered under the cantilever magnet showing how saturation changes with penetration depth. Parameters are the same as Fig. 6: $x_{0\text{p}} = 164\,\text{nm}$, $f_{\text{MW}} = 14.2\,\text{GHz}$, $B_1 = 40\,\mu\text{T}$, cantilever A, and $\mu_0 M_\text{s} = 1800\,\text{mT}$ (*i.e.*, assuming no magnet damage).

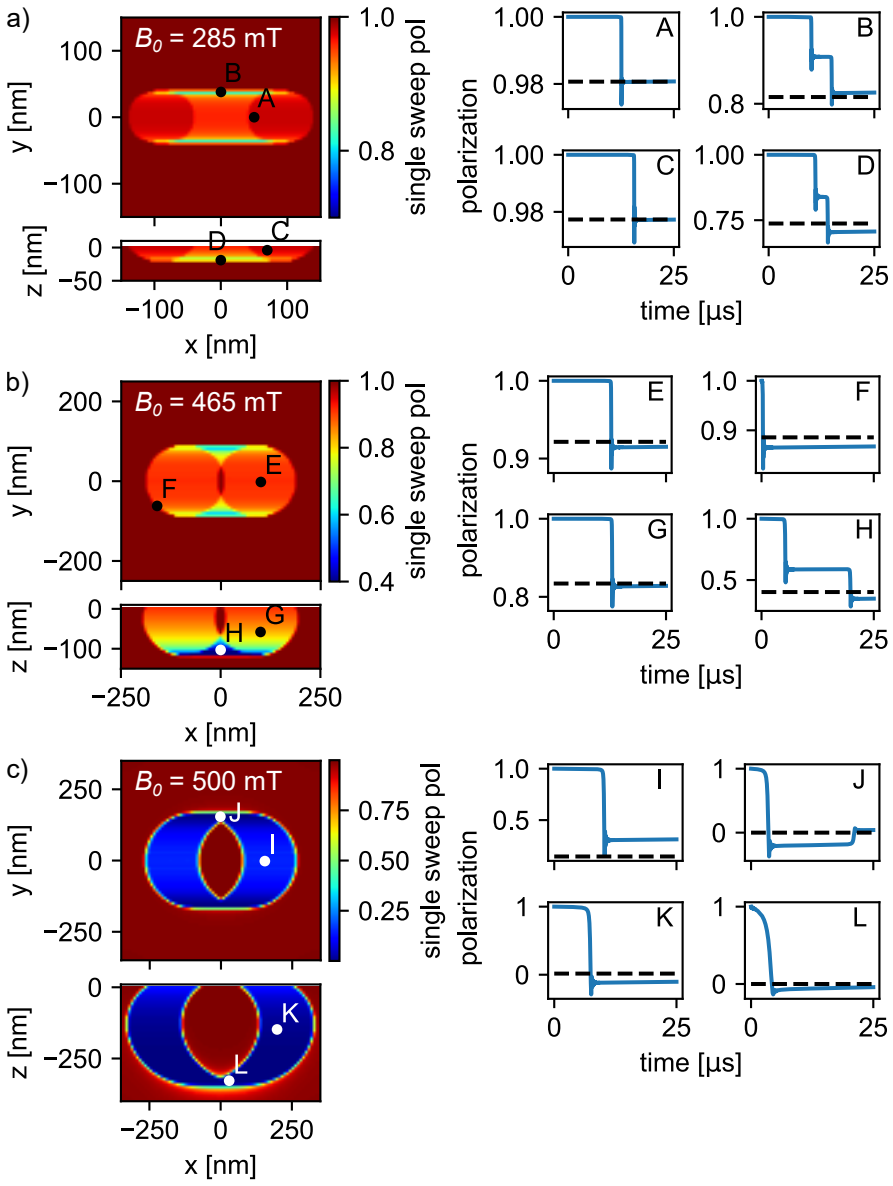

Figure S3: Sample magnetization calculated using Eq. 5 with $B_1 = 40\,\mu\text{T}$ is in reasonable agreement with numerical solutions to the Bloch equations. On the left are cross sections of sample spin polarization following a single pulse, used to calculate the Fig. S2 signal, computed *via* Eq. 7. The plots on the right show the time evolution of sample polarization at sample points indicated in the left-hand polarization cross sections. The dashed lines show the polarization calculated using the Eq. 7 approximation. The blue lines are numerical solutions of the full Bloch equations obtained using the `odeint` method of the Python package SciPy with a time step of 10 ps.

Characterization of Sample T_1 and Microwave Intensity *via* MRFM Meausurements with a Micron-scale Nickel Tip

ESR measurements were performed with a micron-scale nickel tip over a 260 nm thick polystyrene film doped to 40 mM with 4-amino-TEMPO. A waveguide of the same design as the small-tip experiment was used as the sample substrate and MW source. It was found that changing the applied external field moved the sample stage, so the microwave frequency was scanned instead of external field. Microwaves were applied as a half-cycle pulse every second cantilever cycle.

ESR data was collected as a function of tip-sample distance, Fig. S4. In the figure the frequency of the "bulk" resonance is indicated by a dashed line while the frequency of "local" resonance is indicated by a dotted line. The difference in these frequencies divided by the electron gyromagnetic ratio is the tip field. Fitting the resulting tip-field *vs*. distance data,[7] we obtain a tip radius of $r = 4340\,\text{nm}$ and saturation magnetization $B_{\text{sat}} = 560\,\text{mT}$. Some of the plots contain artifacts where the spurious excitation of the cantilever is enhanced at line resonances of the waveguide. We simulated the signal at each tip-sample separation by calculating saturation according to the time-dependent offset method described in the following section and by calculating the resulting frequency shift according to Eq. 8 from Lee *et al.*[8] The simulations are a decent match to the higher frequency local peak. At the bulk resonance MW frequencies, the resonant slice extends outside of the 10 µm width of conductive waveguide centerline. It is unclear how best to treat these spins that experience reduced MW field. In the simulation of Fig. S4, we extend the grid to be 12.5 µm in the x direction, however the match is still imperfect at frequencies close to the bulk resonance.

In Fig. S5(a) we present measurements of sample T_1 using the phase-based protocol of Moore *et al.*[7] The sample has the same concentration of 4-amino-TEMPO radicals. The measured T_1 values are consistent between this laminate sample and the directly deposited film of Moore *et al*. Figure S5(b) shows the resonant slice depth at different MW frequencies. We look for differences

in T_1 at different sample depths from either the metal film or magnet tip but do not observe a statistically significant difference for this micron-scale tip at a tip-sample separation of 1600 nm.

We are interested in the magnitude of the B_1 field experienced by active spins in the sample. We can estimate B_1 by measuring the MW power that passes through the microscope (Fig. S6(a)). We measure microwave power at the waveguide by taking advantage of the symmetry of the cabling of our microscope. Each end of the coplanar waveguide's Arlon board (see Fig. 1) is connected to the microscope exterior through the same type of SMA cabling. We measure losses passing from one end of the microscope to the other and assume half of those losses occur before the center line. In calculating B_1 we assume a uniform current density across the 10 µm width of the centerline.

The time-dependent offset model described in the previous section, and in more detail in an in-preparation manuscript, allows us to measure B_1 more directly by using signal simulations and the known tip field from our nickel magnets. These simulations tell us that the signal *vs*. B_1 curve increases steeply under two conditions. The first steep rise corresponds to reaching the saturation condition for spins irradiated in the presence of the moving tip. The second steep rise occurs when power broadening starts saturating spins beyond the resonant slice.

In fitting the signal *vs*. B_1 data, Fig. S6(b), we make the assumption that observed knee represents the saturation of the first steep portion of the curve. The simulation accurately captures the non-monotonic increase in signal with irradiation power, with a few deviations. At low B_1 the observed signal is larger than the simulation possibly due to the quick saturation of spins that pass through resonance as tip motion slows near the apex of motion.

Another potential source of disagreement between calculated and measured signals at large microwave power is a reduction in sample polarization due to sample heating. In Fig. 4 of Ref. 7, the potential effects of spurious excitation are cancelled by an off-resonance control experiment. While we might expect the signal of Fig. 4 to continue to increase due to power broadening, instead we see the signal plateau or even taper. A similar effect might be expected in the present experiment.

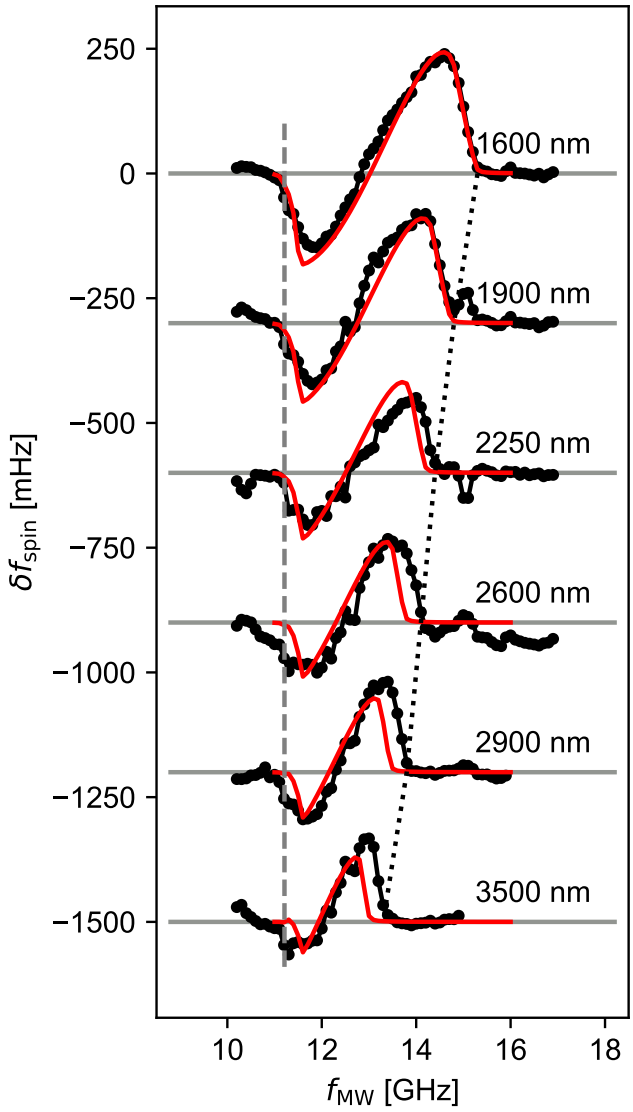

Figure S4: The measured force-gradient detected electron-spin resonance signal of 4-amino-TEMPO collected with a micron-scale spherical tip is in excellent agreement with the calculated signal. Black circles are experimental data. Red lines are a simulation using the mrfmsim package, with saturation calculated according to Eq. 7 and frequency shift calculated according to Eq. 8 from Lee *et al.*[8] The gray dashed line is the microwave frequency of the bulk resonance, and the black dotted line is the largest frequency at which signal was detected for each tip sample separation. Experimental parameters: $r = 4340\,\mathrm{nm}$, $B_0 = 400\,\mathrm{mT}$, zero-to-peak amplitude $= 164\,\mathrm{nm}$, $f_0 = 3100\,\mathrm{Hz}$, $k_\mathrm{c} = 0.6\,\mathrm{mN\,m^{-1}}$, $\mu_0 M_s = 560\,\mathrm{mT}$, $t_\mathrm{pulse} = 150\,\mu\mathrm{s}$. Simulation parameters: Grid extent $(L_x, L_y, L_z) = (10\,\mu\mathrm{m}, 20\,\mu\mathrm{m}, 260\,\mathrm{nm})$; grid size $(\Delta x, \Delta y, \Delta z) = (25\,\mathrm{nm}, 25\,\mathrm{nm}, 10\,\mathrm{nm})$; and $B_1 = 40.0\,\mu\mathrm{T}$.

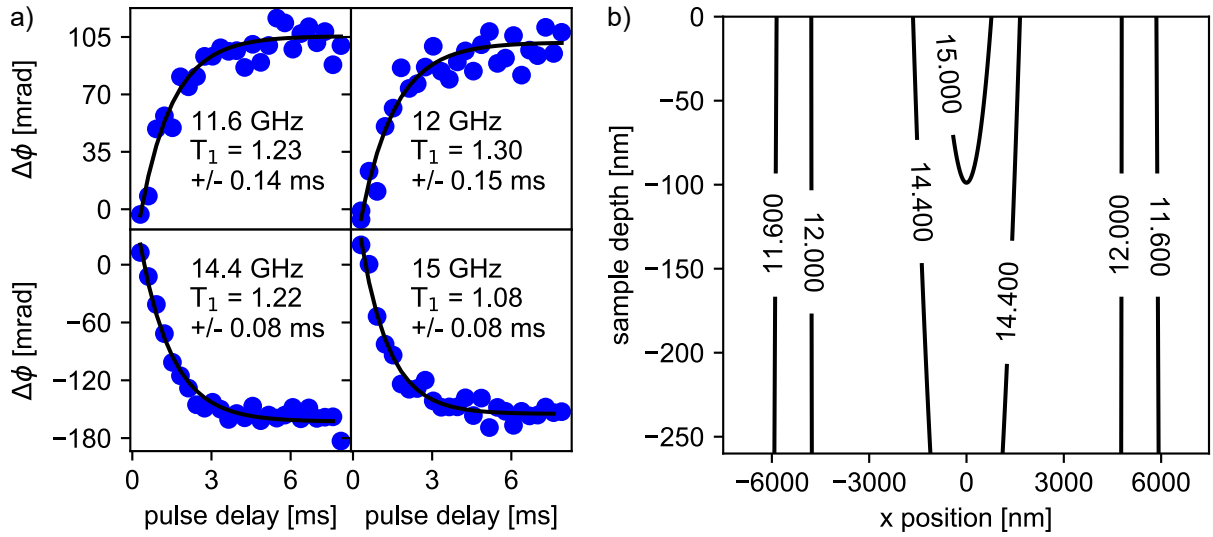

Figure S5: Measured T_1 versus frequency with micron-scale Ni tip performed on a 260 nm-thick laminate film doped to 40 mM with 4-amino-TEMPO. (a) T_1 measured as a force-gradient MRFM signal detected following Moore.[7] Experimental parameters: $B_0 = 400\,\mathrm{mT}$, tip radius $r = 4340\,\mathrm{nm}$, and tip-sample separation $h = 1600\,\mathrm{nm}$. (b) Simulated resonant slice profile versus f_{MW} in GHz.

From the Fig. S6 data we estimate a coil constant of $8\,\mu\mathrm{T}^2\mu\mathrm{W}^{-1}$ (per unit power) or $2.8\,\mu\mathrm{T}\,\mu\mathrm{W}^{-1/2}$ (per unit amplitude). Using Ohm's law, assuming a $50\,\Omega$ impedance and a $10\,\mu$m-wide centerline, we expect the current density to be $14.14\,\mathrm{Am}^{-1}\mu\mathrm{W}^{-1/2}$. Multiplying this current density by the vacuum permeability divided by two we obtain an estimated coil constant of $96\,\mu\mathrm{T}^2\mu\mathrm{W}^{-1}$ (per unit power) or $8.9\,\mu\mathrm{T}\,\mu\mathrm{W}^{-1/2}$ (per unit amplitude). The observed coil constant, per unit amplitude, is a factor of three smaller than the calculated one. Agreement between simulated and observed coil constants would improve if the actual cable-conduction losses at 14.4 GHz were larger than the -17 dB estimate obtained by averaging the measured values at 14 GHz and 15 GHz.

The estimated coil constant suggests we should be able to get well above the low-B_1 limit within the dynamic range of our microwave amplifier and radiation source. Even with our estimated 17 dB of losses through the microscope cabling we expect $B_1 \sim 40\,\mu\mathrm{T}$ at our 10 dBm standard input power.

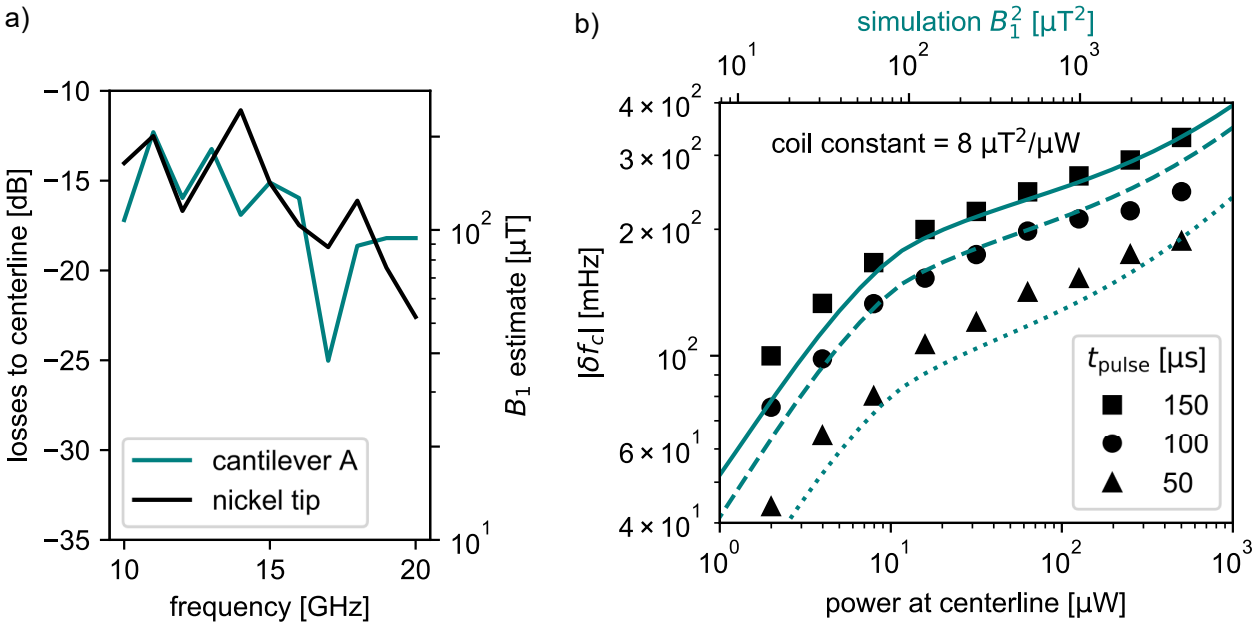

Figure S6: Estimate of B_1 from measured MW power and micron-tip MRFM signal. (a) Left axis: measured losses between MW source and the waveguide centerline at 4K for two different experimental runs. Right axis: estimated transverse field B_1, calculated from the measured power and centerline dimensions assuming 10 dBm of power from the MW source. (b) Coil constant simulation for MRFM ESR with a large nickel tip at $f_{MW} = 14.4\,\text{GHz}$ (local peak) and $B_0 = 400\,\text{mT}$, 1600 nm tip-sample separation with a 164 nm zero-to-peak amplitude. Triangles, circles and squares represent ESR data obtained with 50, 100, and 150 μs MW pulses respectively. The signal is plotted against estimated MW power reaching the centerline after the losses shown in (a). Teal lines represent simulations using the time-dependent offset method with B_1^2 from the upper x-axis to calculate spin saturation, and calculating frequency shift using the second derivative of the tip field in the direction of tip motion (Eq. 8 in Ref. 8). We use the "knee" of the three saturation curves to align the two x axes and extract our estimate of the coil constant. Simulation parameters: magnet radius = 4340 nm, $B_{sat} = 560\,\text{mT}$.

Analysis of Signal Loss from Low B_1

Since pure damage models fail to fully explain the tip field observations at small tip-sample separations, let us consider alternative explanations. The Fig. S6 measurements demonstrate that our apparatus can deliver a rotating-frame B_1 as big as 200 μT, significantly larger than the $B_{\text{sat}} = 1/\gamma_e\sqrt{T_1 T_2} = 0.24\,\mu\text{T}$ required to saturate the sample's electron spins. In this section we show that to saturate sample spins beneath a moving tip, B_1 must be considerably larger than B_{sat}. This large B_1 is required to compensate for the enormous time-dependent resonance offsets experienced by spins below the moving cantilever tip.

Previously, we presented equations used to calculate partial saturation. For the main text we assumed $B_1 = 40\,\mu\text{T}$ based on the measured values from the previous section taken with a micron-scale tip. In the following paragraphs we consider what signal we would expect in the case where B_1 is reduced to the weak-irradiation limit.

As shown in Figure S7 the model heavily penalizes B_1 values in the weak-irradiation limit. Even at the bulk external field value $B_0 = 500\,\text{mT}$, surface spins at $h = 32\,\text{nm}$ are less than 2% saturated by a single microwave pulse at $B_1 = 4\,\mu\text{T}$. This translates to a greatly reduced average saturation in Fig. S7(b-d). Repeated application of microwaves every 200 μs allows for saturation to accumulate and spins are $\sim 10\%$ saturated on average at $B_0 = 500\,\text{mT}$. Figure S7(a) shows a moving-tip simulation with the same parameters as Fig. 6 from the main text; the signal is reduced in the moving-tip experiment by more than a factor of 20. The signal is still much broader than we observe experimentally, and even in the tapered region at the highest tip-field values we still expect $\sim 1\,\text{mHz}$ of signal.

Poor saturation of spins through this mechanism could certainly lead to a reduction in observed tip field. However, for an undamaged magnet, we would not expect a result as abrupt as seen in Fig. 6(a). For $B_0 = 500\,\text{mT}$, the resonant slice still has a significant diameter so the number of active spins does not change dramatically with external field and neither should the factor of B_{zx} used to determine saturation (Eq. 6). Even with this mechanism, a large proportional change in

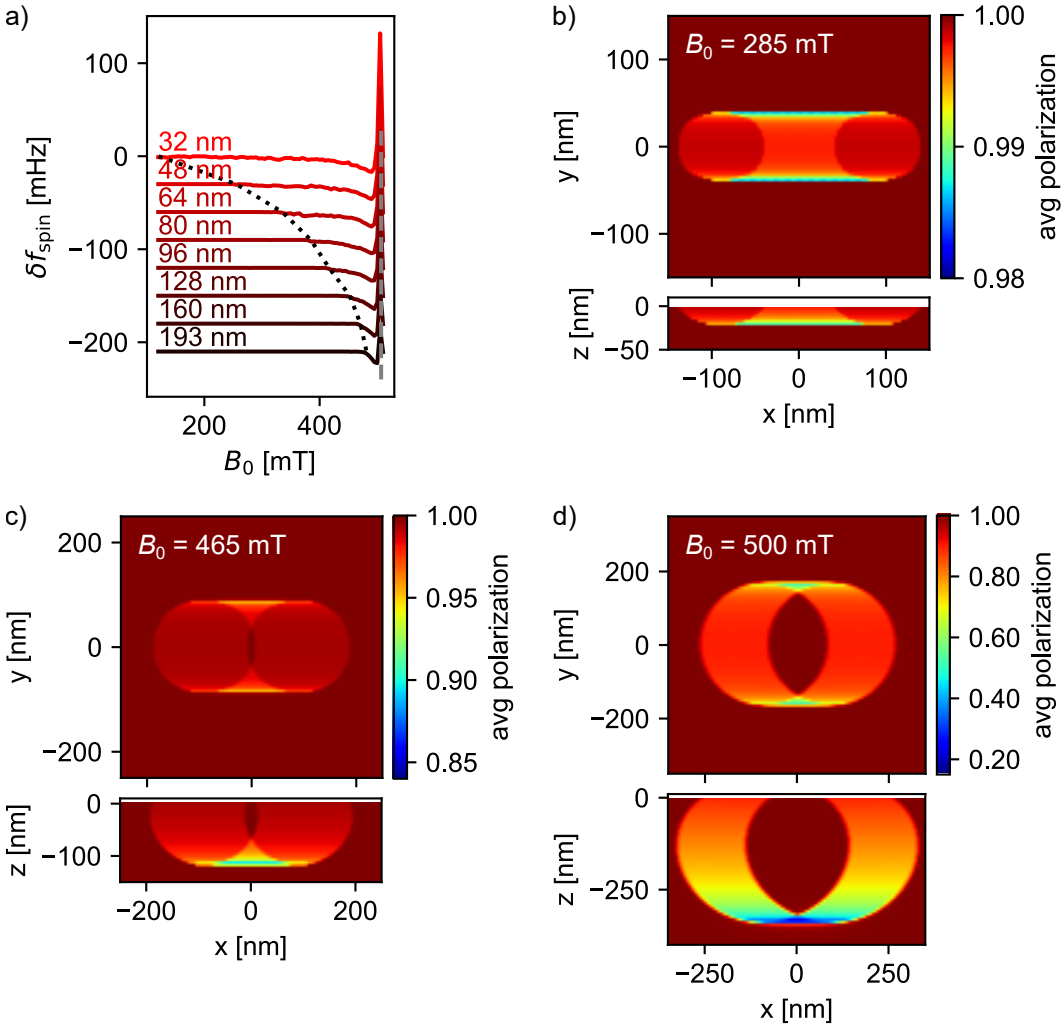

Figure S7: Impact of large time-dependent resonance offset on spin polarization and MRFM-ESR signal in the weak-irradiation limit, $B_1 = 4\,\mu\text{T}$. (a) Same simulation as in Fig. 6(b) but with $B_1 = 4\,\mu\text{T}$ (*i.e.* cantilever A, $x_{0p} = 164\,\text{nm}$, with a 25 µs MW pulse). (b-d) Simulations of Fig. S2(b-d) with $B_1 = 4\,\mu\text{T}$.

signal size indicates a large proportional change in tip field. For an undamaged magnet, we expect the gradual taper we see in Fig. S7(b).

We could also consider a hybrid model with some tip damage and the effects of reduced saturation to point out another inconsistency with an explanation based on insufficient B_1. Figure S8 shows one such model. We simulate with a 15 nm damage layer in the magnet and apply our time-dependent resonance offset equations with a $B_1 = 4\,\mu\text{T}$. A model like this could be made to match the local peak with decent accuracy if parameters were carefully tailored. However, it fails to match the bulk peak of the signal, where we would expect the tip field to change much more slowly in time. We could attribute this difference to spin diffusion, which could happen much more easily where the tip field is weak.

Figure S8(b) and (c) show a problem with this model in explaining our results. If we are in a regime where saturation from a single microwave pulse is $\propto B_1^2$, then increasing B_1 should have a dramatic effect on signal size, as seen in the simulation in Fig. S8(b). Yet experimentally we observe the signal to be essentially B_1-independent over a factor of 10 increase in MW power, Fig. S8(c).

We conclude that we need to look for other mechanisms to explain the observed tip field *vs*. tip-sample separation data and the dependence of signal on B_0 (or ω_{res}) and B_1. Poor spin saturation because of limited B_1 and a rapidly changing tip field during irradiation fails as an explanation because (1) the measured power through the microscope suggests we should be well out of the weak-B_1 regime and (2) experiments varying microwave power show a weak dependence on input power, which is not the expected behavior in the weak-B_1 regime.

Sample Spin-lattice Relaxation Due to the Sample Coating

To ascertain the effect of current fluctuations in the gold top contact on sample T_1, we performed a four-point probe measurement of the resistivity of a test sample and used Eq. 3 from Ariyaratne *et*

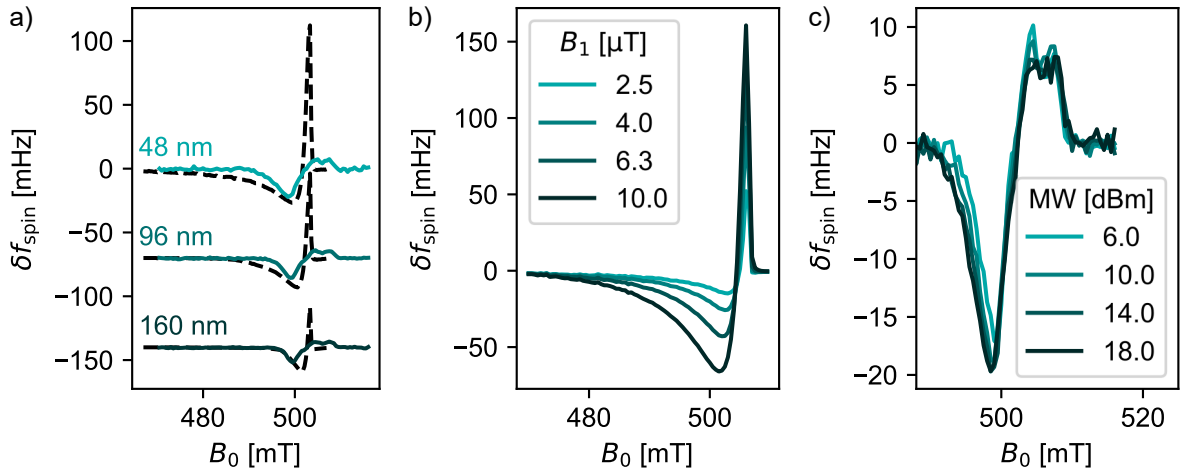

Figure S8: Hybrid signal-loss model involving both tip damage and reduced saturation from large time-dependent resonance offset. (a) Simulation of electron-spin resonance signal *vs*. tip-sample separation for a magnet with a 15 nm damage layer and $B_{sat} = 1.02\,\mathrm{T}$ (black dashes) and experimental data (teal) (b) Simulation of the same tip model from (a) with varied B_1, showing that predicted signal amplitude is highly dependent on B_1. If we expanded the y-axis we would see that the observed tip-field is not strongly B_1-dependent. (c) Experiment with varied MW power showing minimal broadening of the signal and increase in amplitude over a factor of 10 increase in MW power. Zero-to-peak amplitude was 164 nm and $t_{pulse} = 25\,\mu\mathrm{s}$. For the simulation in (a) B_1 is assumed to be $4.0\,\mu\mathrm{T}$. For (b) and (c) the tip-sample separation was 55 nm.

al.[9] to estimate the resulting sample T_1 times (Fig. S9).

A 200 nm thick polystyrene (Sigma-Aldrich, lot MKBF5599V, $M_n = 186,600$, $M_w/M_n = 1.02$) film was spin-coated onto a $10\,\mathrm{mm} \times 2\,\mathrm{mm}$ Si substrate from a 40 mg/mL solution in anhydrous p-xylene (Sigma-Aldrich, $> 99\%$, batch 39696TK). A 12 nm layer of gold was electron-beam deposited on top of the polymer at a rate of $1\,\mathrm{Å\,s^{-1}}$ using the CVC SC4500 E-gun Evaporation System at the Cornell Nanoscale Facility. Part of the substrate was masked off to define the dimensions of the deposited film. A line of wirebonds was made from the 4-point-probe sample holder to the Au film. A geometry factor[10] GF was calculated for each sample based on the film dimensions and probe spacings (see Table S4).

Measurements were taken on a Quantum Design PPMS Physical Property Measurement System with a measurement current of $100\,\mu\mathrm{A}$. The temperature was scanned at a rate of $5\,\mathrm{K\,min^{-1}}$ from 300 K down to 4 K. The values measured below 10 K were averaged over the multiple samples to estimate a resistivity of $111.9\,\mathrm{n\Omega\,m}$ at 4 K. Measured values were consistent with literature

Table S4: Sample parameters for sheet-resistance measurements. Length l and width w refer to the dimensions of the e-beam-deposited film and the resulting geometry factor, GF. Probe electrodes were wirebonded to the sample in a line. The spacing between the $+I$ and $+V$, $+V$ and $-V$, and $-V$ and $-I$ electrodes are denoted as s_1, s_2, and s_3 respectively.

sample	s_1 [mm]	s_2 [mm]	s_3 [mm]	l [mm]	w [mm]	GF
1	1.1	1.3	1.2	4.1	2.1	0.39
2	1.6	1.4	1.0	6.1	2.1	0.35
3	1.3	1.5	1.3	6.0	2.1	0.33

values at room temperature[11] and 4 K.[12,13] Figure S9(b) shows the estimated T_1 *vs.* sample depth. We conclude that the sample radicals would have to be ~ 1 Å from the metal film to reduce their T_1 to less than a cantilever period. As a result we would not expect the MRFM signal to be noticeably impacted by the 12 nm-thick gold film.

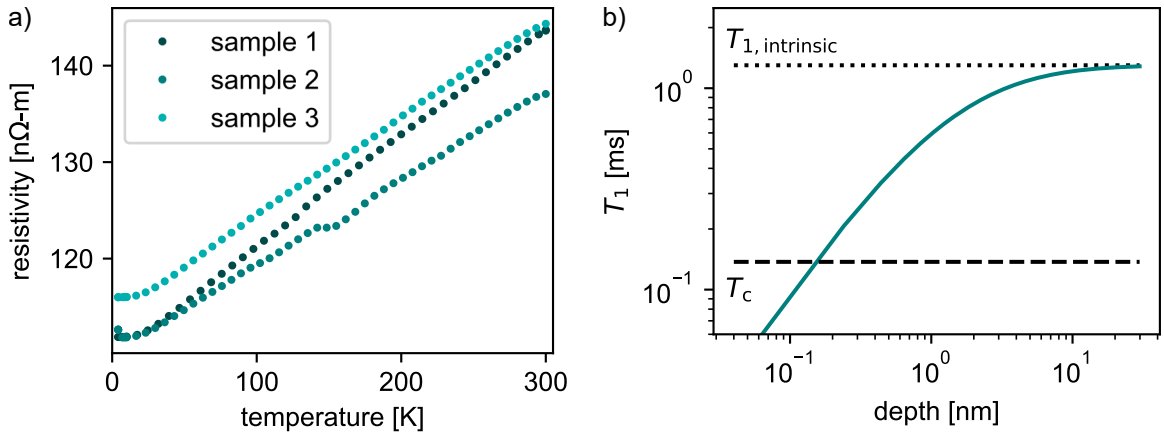

Figure S9: Measured top-contact conductivity and estimated reduction in T_1 of nearby spins. (a) Measured four-point-probe resistivity of laminate film versus temperature. (b) The resistivity values between $T = 4$ K and 10 K were averaged and used with the equations derived in Ariyaratne *et al.*[9] to estimate relaxation due to conductivity fluctuations in the nearby gold film and predict the indicated effective T_1 versus distance from the metallic top contact.

Sample Spin-lattice Relaxation from Tip Magnetization Fluctuations

Another source of spin relaxation is thermomagnetic fluctuations of the cantilever magnet.[1,14–16] We estimated the power of these fluctuations following Ng *et al.*[1] First we measured the quality factor *vs*. tip field, from a ringdown measurement at each field step during magnetometry (Fig. S10). We calculated the magnetic dissipation by subtracting off the dissipation at $B_0 = 0\,\mathrm{T}$. We used the resulting magnetic dissipation to calculate the spectral density of transverse tip magnetic moment fluctuations at the cantilever frequency, $S_\mu(f_\mathrm{c})$.

We can calculate the fluctuating magnetic field felt by an individual spin due to the tip according to $S_B = S_\mu B_\mathrm{tip}^2/4\mu^2$. For B_tip we use 10 mT, because that is a plausible value at which the T_1 would have to be significantly less than the cantilever period in order to see the signal we observe. For μ we assume the value for the undamaged tip in Table S3, because it has the most plausible spring constant. If we use the case with the most drastic tip damage we would expect a $\sim$6-fold increase in S_B and the calculated spin relaxation rate. The electron-spin relaxation rate depends on the spectral density of transverse magnetic field fluctuations at the *Larmor* frequency, $T_1^{-1} = \gamma_\mathrm{e}^2 S_B(f_\mathrm{L})$ with γ_e the electron gyromagnetic ratio and $f_\mathrm{L} = \gamma_\mathrm{e} B_0 \sim 14\,\mathrm{GHz}$ the electron Larmor frequency. Cantilever magnetic dissipation measures the spectral density of transverse magnetic field fluctuations at the *cantilever* frequency, $f_\mathrm{c} \sim 7.3\,\mathrm{kHz}$.

In Fig. S10(b), we calculate the T_1 of electron spins in the sample assuming $S_B(f_\mathrm{L}) \approx S_B(f_\mathrm{c})$. We consider the resulting T_1 to be an upper bound for the electron T_1 because the electron Larmor frequency is much closer than the cantilever frequency to the tip's ferromagnetic resonance frequencies.

The T_1 values shown on the right hand axis of Fig. S10(b) would have a noticeable impact on our observed signal. As T_1 falls below the cantilever period we are no longer able to accumulate saturation between cantilever cycles and in more extreme cases would expect significant relaxation

during a cantilever cycle or even during a MW pulse. An undamaged tip would be expected to produce B_{tip} in excess of 300 mT for the nearest spins, which could therefore have T_1 values another three orders of magnitude lower. The fact that we start to observe a reduction in T_1 at the same field where the signal seems to taper suggests that magnetic-fluctuation-induced relaxation is of the correct magnitude to explain our reduced signal.

We also plot quality factor *vs.* external field data for cantilever B. We observe less magnetic dissipation for cantilever B, $5.8 \times 10^{-15}\,\text{kg}\,\text{s}^{-1}$ at 0.5 T, compared to the $2.7 \times 10^{-15}\,\text{kg}\,\text{s}^{-1}$ at 0.5 T from cantilever A. As a result of this reduced magnetic friction, and because the cantilever-B experiment was carried out at higher field, we expect fewer effects from T_1 shortening. Still, at higher tip field values, we would expect to see shortening. At $B_{\text{tip}} = 100\,\text{mT}$, we expect fluctuations to be $100\times$ as large, and we would see a signal reduction.

Ongoing work seeks to use micromagnetics simulations to determine the magnitude of the fluctuating field at the Larmor frequency and to use analytical approximations and numerical calculations to estimate the contribution of spins with sub-cantilever cycle T_1 times to the gradient-detected MRFM signal.

Eddy Current Damping

We can estimate the dissipation from eddy currents using the measured properties of our experiment. We will follow the derivation in Reitz[17] of the drag force on a magnet moving over a thin conducting plate. Because of the high aspect ratio of our magnets and the comparatively small tip-sample separation (see Table 1) we will use the monopole approximation to calculate the drag force, F_D:

$$F_D = (w/v)\,F_L, \tag{8}$$

with lift force

$$F_L = (\mu_0 q^2/16\pi z_0^2)[1 - w/(v^2 + w^2)^{1/2}]. \tag{9}$$

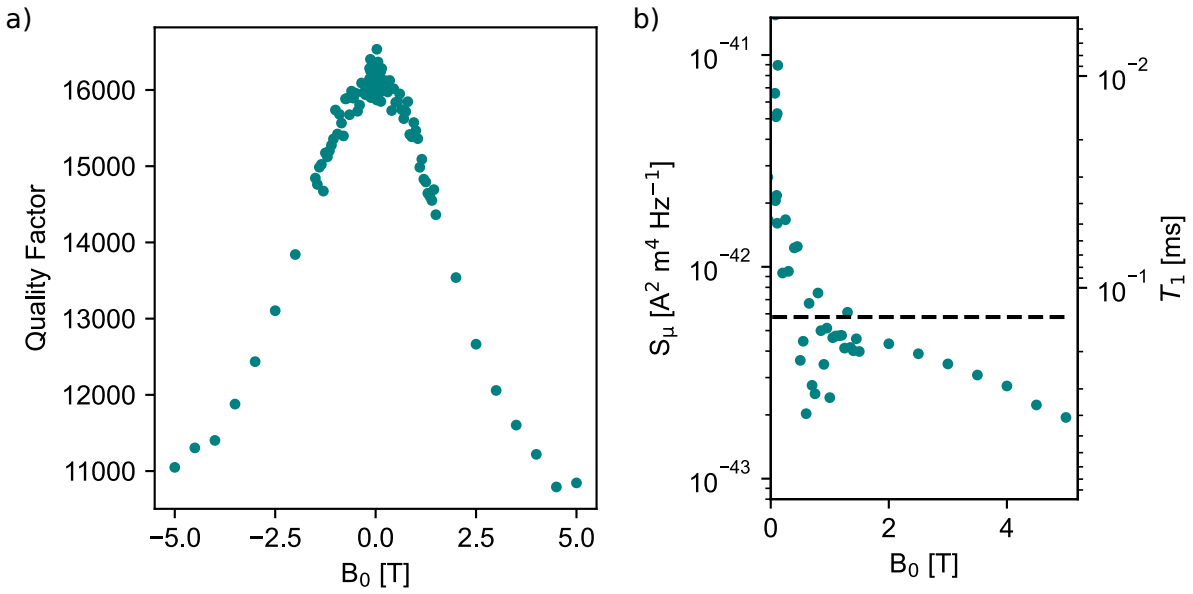

Figure S10: Predicting tip magnetic-moment fluctuations and the resulting sample T_1 from measured cantilever damping in an applied magnetic field. (a) Quality factor *vs*. external field of cantilever A. (b) Left axis: Spectral density of transverse magnetization fluctuations inferred from magnetic friction. Right axis: The electron spin-lattice relaxation rate T_1 from equivalent transverse magnetization fluctuations occurring at the electron Larmor frequency.[1] The dashed line is the cantilever period in milliseconds. To calculate T_1 we assumed no damage layer and used the corresponding μ value from Table S3. B_{tip} was taken to be 10 mT, the value at which the ESR signal starts to taper in Fig. 6

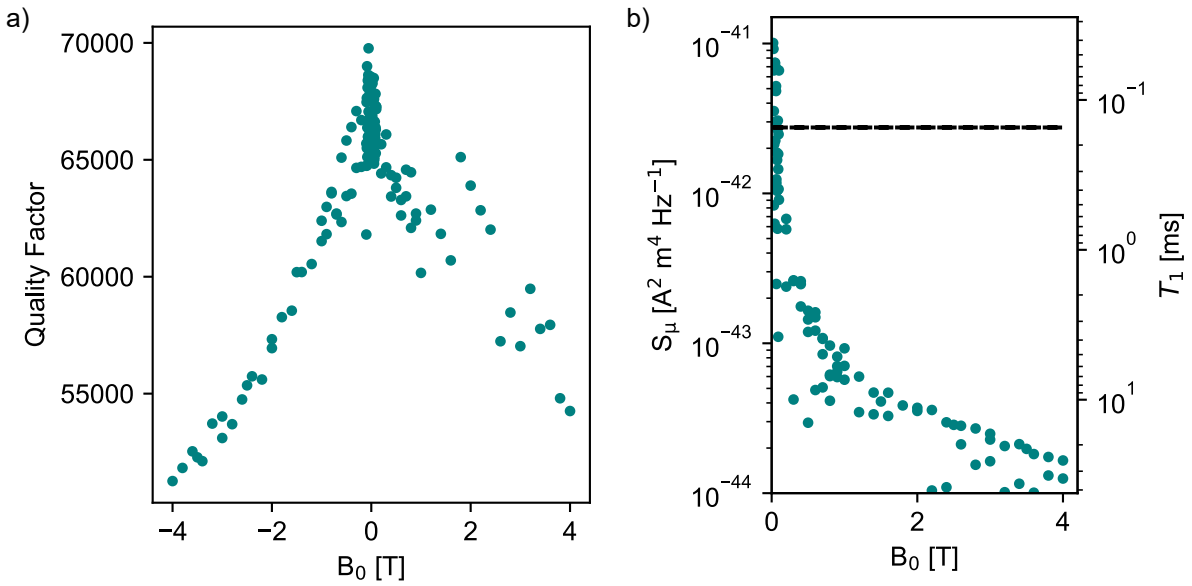

Figure S11: Predicting tip magnetic-moment fluctuations and the resulting sample T_1 from measured cantilever damping in an applied magnetic field. (a) Quality factor *vs*. external field of cantilever B. (b) Left axis: Spectral density of transverse magnetization fluctuations inferred from magnetic friction. Right axis: The electron spin-lattice relaxation rate T_1 from equivalent transverse magnetization fluctuations occurring at the electron Larmor frequency.[1] The dashed line is the cantilever period in milliseconds. To calculate T_1 we assumed no damage layer and used the corresponding μ value from Table S2. B_{tip} was taken to be 10 mT.

with w a parameter with units of velocity,

$$w = \frac{2}{\mu_0 \sigma \delta}. \tag{10}$$

Here $\sigma = 8.936 \times 10^{-3}\,\mathrm{n\Omega^{-1}\,m^{-1}}$ is the film conductivity, measured in Fig. S9, and $\delta = 12\,\mathrm{nm}$ is the film thickness. We will use 30 nm as the tip-sample separation. The tip velocity at its peak is $v = \omega_c x_{0-\mathrm{pk}} = 7.5 \times 10^{-3}\,\mathrm{m\,s^{-1}}$ for a zero-to-peak amplitude of $x_{0-\mathrm{pk}} = 164\,\mathrm{nm}$. We calculate q by using the magnet model with the largest magnetic moment from Table S3 and dividing by the length, 1500 nm, to get $5.27 \times 10^{-9}\,\mathrm{A\,m}$. To calculate dissipation, we perform a Taylor series expansion of the drag force equation around $v_0 = 0$ and obtain the first-order term

$$F_D = \frac{\mu_0 q^2 v}{32\pi w z_0^2} + O[v]^3. \tag{11}$$

Because w is so much larger than v, the higher order terms are much smaller than the first order term. Additionally, we expect the lift force to be much smaller than drag force. We extract the coefficients to obtain the dissipation,

$$\Gamma = \frac{\mu_0 q^2}{32\pi w z_0^2}. \tag{12}$$

Plugging in the variables we obtain $\Gamma = 26\,\mathrm{aN\,s\,m^{-1}}$. This is orders of magnitude less than the intrinsic dissipation of our cantilevers at 4 K, which are in the pN s $\mathrm{m^{-1}}$ range.

We did not attempt to measure the eddy current dissipation during our small tip experiments, but dissipation over metal appeared to be smaller than over polystyrene at similar tip-sample separations. Previously we have attempted to measure eddy current damping with magnet-tipped cantilevers produced through the same protocol (see Figure 6 of Longenecker *et al.*[18]). The effects appeared to be small.

Roughness of the Transferred Film

We characterized the surface roughness of the laminate sample with an Asylum-MFP3D-Bio-AFM-SPM system operating in tapping mode with a Nanosensors SSS-NCHR-SPL cantilever ($k_c = 42\,\mathrm{N\,m^{-1}}$, $f_c = 299.8\,\mathrm{kHz}$, S/N 66929F8L835). The AFM scan was 268×268 points with a 0.6 Hz scan rate. The sample roughness is less than 1 nm in most places with some added roughness from bumps or wrinkles. Figure S12 shows representative data. Bumps could be reduced with more filtration of the spin solution or by operating in a clean room to reduce dust. Wrinkles may be due to difficulty in manually applying a polymer film completely flush to the waveguide or water trapped between the waveguide and sample film.[19]

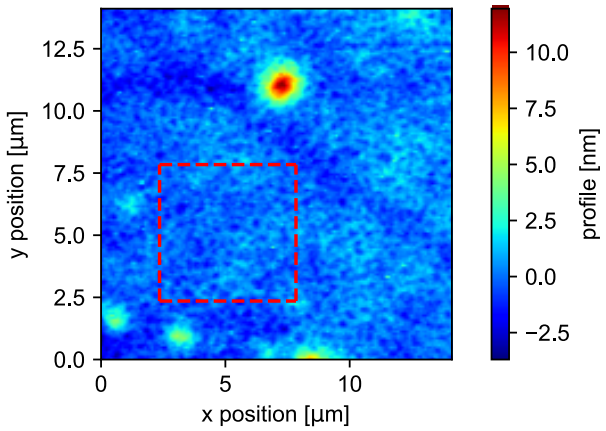

Figure S12: Tapping-mode atomic force microscope topography of a region of the laminate sample over the waveguide ground plane. The waveguide centerline was located $<100\,\mu\mathrm{m}$ in the x direction from the scan area. The root-mean-square surface roughness is 0.66 nm and 1.10 nm over the boxed area and whole area, respectively.

Inductive ESR Measurements

We used the `stats.ttest_ind` method from the python SciPy python package to perform a Welch's t-test on the pairwise differences between the mean integrated electron spin-echo signal from samples with no gold deposition, our "standard deposition" rate of $1\,\mathrm{Å\,s^{-1}}$, and a "slow deposition" rate of $0.1\,\mathrm{Å\,s^{-1}}$. The results are summarized in Table S5.

We multiplied each ESR signal by the total mass of the toluene solvent, and divided by (1) the integral of the resonator reference measurement taken immediately prior to sample measurement and (2) the average thickness of the dissolved film as determined by stylus profilometry. We integrated these corrected signals and normalized them so that the "no gold film" treatment had an average integrated signal of 1.0 and subjected the resulting normalized signals to statistical significance testing. A Bonferroni correction was applied to prevent a type I error from performing multiple comparisons, *i.e.* the adjusted p-values were calculated by multiplying the raw p-values by 3, the total number of comparisons performed.

We find that the integrated spin-echo signal of the sample with no deposited gold was different from both treatments with e-beam-deposited gold, significant at the $p = 0.05$ level. We are also interested in whether changing the deposition rate impacts the depth of sample damage. While the means were different, with the slow gold deposition having a smaller signal, the difference was not significant at the $p = 0.05$ level.

If we assume that spins were uniformly destroyed in the damage layer, we can estimate the thickness. We take the signals and adjust them for solvent volume and resonator sensitivity. We take the thickness of the remaining undamaged sample to be the thickness of the no-deposition sample scaled by the ratio of signal of e-beam treatment of interest and the signal of the no-deposition sample. Using this approach we estimate a damage layer of 19 nm for the standard deposition and 25 nm for the slow deposition treatment.

Table S5: Welch's t-test of differences in inductively detected electron spin-echo signal for samples with no gold deposition, our "standard deposition" rate of $1\,\text{Å}\,\text{s}^{-1}$, and a "slow deposition" rate of $0.1\,\text{Å}\,\text{s}^{-1}$. The Bonferroni correction was applied to calculate the adjusted p-values.

group 1	group 2	mean diff.	p-adj.	reject
no film	slow dep.	−0.5849	0.0215	True
no film	stand. dep.	−0.3848	0.0187	True
slow dep.	stand. dep.	0.2001	0.3889	False

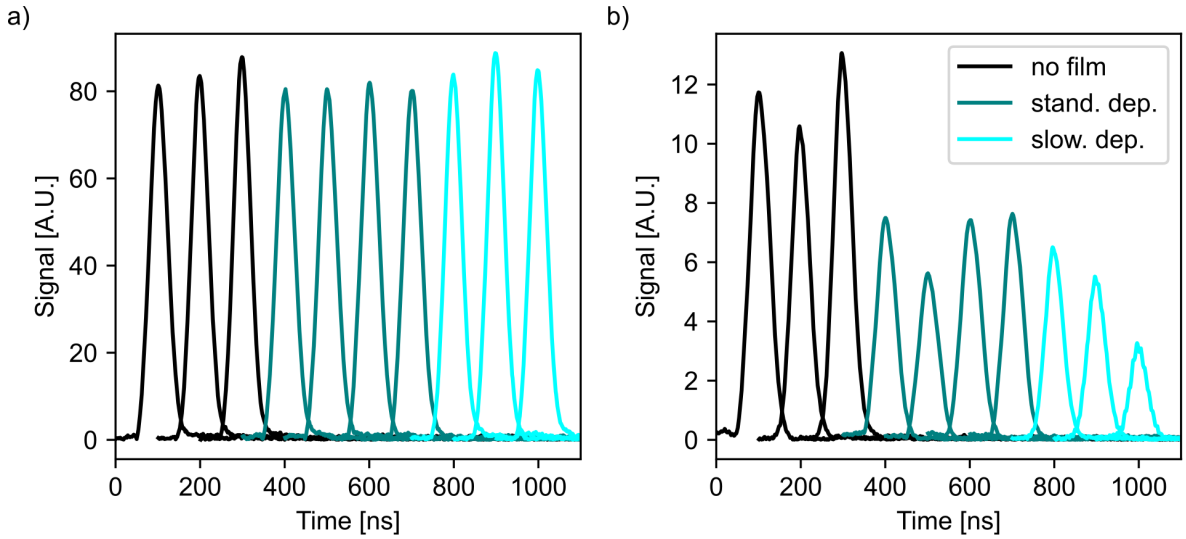

Figure S13: Raw inductively-detected signal from the electron spin echo measurement used to produce Fig. 4. (a) Reference signal taken using a Cr^{3+} ESR standard before each sample measurement. (b) Measurements of test samples. Runs are color-coded by treatment.

References

(1) Ng, T. N.; Jenkins, N. E.; Marohn, J. A. Thermomagnetic Fluctuations and Hysteresis Loops of Magnetic Cantilevers for Magnetic Resonance Force Microscopy. *IEEE Trans. Mag.* **2006**, *42*, 378–381.

(2) Marohn, J. A.; Fainchtein, R.; Smith, D. D. An Optimal Magnetic Tip Configuration for Magnetic-Resonance Force Microscopy of Microscale Buried Features. *Appl. Phys. Lett.* **1998**, *73*, 3778–3780.

(3) Aharoni, A. Demagnetizing Factors for Rectangular Ferromagnetic Prisms. *J. Appl. Phys.* **1998**, *83*, 3432–3434.

(4) Whitney, T. M.; Searson, P. C.; Jiang, J. S.; Chien, C. L. Fabrication and Magnetic Properties of Arrays of Metallic Nanowires. *Science* **1993**, *261*, 1316 – 1319.

(5) Thurn-Albrecht, T.; Schotter, J.; Kästle, G. A.; Emley, N.; Shibauchi, T.; Krusin-Elbaum, L.; Guarini, K.; Black, C. T.; Tuominen, M. T.; Russell, T. P. Ultrahigh-Density Nanowire Arrays Grown in Self-Assembled Diblock Copolymer Templates. *Science* **2000**, *290*, 2126 – 2129.

(6) Hickman, S. A. Batch Fabrication of Cantilevered Magnetic Nanorods on Attonewton-Sensitivity Silicon Oscillators for Magnetic Resonance Force Microscopy. Ph.D. thesis, Cornell University, Ithaca, New York, 2010.

(7) Moore, E. W.; Lee, S.-G.; Hickman, S. A.; Wright, S. J.; Harrell, L. E.; Borbat, P. P.; Freed, J. H.; Marohn, J. A. Scanned-Probe Detection of Electron Spin Resonance from a Nitroxide Spin Probe. *Proc. Natl. Acad. Sci. U.S.A.* **2009**, *106*, 22251–22256.

(8) Lee, S.-G.; Moore, E. W.; Marohn, J. A. A Unified Picture of Cantilever Frequency-Shift Measurements of Magnetic Resonance. *Phys. Rev. B* **2012**, *85*, 165447.

(9) Ariyaratne, A.; Bluvstein, D.; Myers, B. A.; Bleszynski Jayich, A. C. Nanoscale Electrical Conductivity Imaging Using a Nitrogen-Vacancy Center in Diamond. *Nat Commun* **2018**, *9*, 194.

(10) Perloff, D. S. Four-Point Sheet Resistance Correction Factors for Thin Rectangular Samples. *Solid-State Electronics* **1977**, *20*, 681 – 687.

(11) Gilani, T.; Rabchuk, D. Electrical Resistivity of Gold Thin Film as a Function of Film Thickness. *Can. J. Phys.* **2018**, *96*, 272 – 274.

(12) de Vries, J. W. C. Resistivity of Thin Au Films as a Function of Grain Diameter and Temperature. *J. Phys. F: Met. Phys.* **1987**, *17*, 1945 – 1952.

(13) Bahamondes, S.; Donoso, S.; Ibañez-Landeta, A.; Flores, M.; Henriquez, R. Resistivity and Hall Voltage in Gold Thin Films Deposited on Mica at Room Temperature. *Applied Surface Science* **2015**, *332*, 694 – 698.

(14) Hannay, J. D.; Chantrell, R. W.; Rugar, D. Thermal Field Fluctuations in a Magnetic Tip / Implications for Magnetic Resonance Force Microscopy. *J. Appl. Phys.* **2000**, *87*, 6827–6829.

(15) Stipe, B. C.; Mamin, H. J.; Yannoni, C. S.; Stowe, T. D.; Kenny, T. W.; Rugar, D. Electron Spin Relaxation near a Micron-Size Ferromagnet. *Phys. Rev. Lett.* **2001**, *87*, 277602.

(16) Stipe, B. C.; Mamin, H. J.; Stowe, T. D.; Kenny, T. W.; Rugar, D. Magnetic Dissipation and Fluctuations in Individual Nanomagnets Measured by Ultrasensitive Cantilever Magnetometry. *Phys. Rev. Lett.* **2001**, *86*, 2874–2877.

(17) Reitz, J. R. Forces on Moving Magnets due to Eddy Currents. *J. Appl. Phys.* **1970**, *41*, 2067–2071.

(18) Longenecker, J. G.; Mamin, H. J.; Senko, A. W.; Chen, L.; Rettner, C. T.; Rugar, D.; Marohn, J. A. High-Gradient Nanomagnets on Cantilevers for Sensitive Detection of Nuclear Magnetic Resonance. *ACS Nano* **2012**, *6*, 9637–9645.

(19) Kim, H. H.; Lee, S. K.; Lee, S. G.; Lee, E.; Cho, K. Wetting-Assisted Crack- And Wrinkle-Free Transfer of Wafer-Scale Graphene Onto Arbitrary Substrates Over a Wide Range of Surface Energies. *Adv. Funct. Mater.* **2016**, *26*, 2070 – 2077.